

Structure and superconducting properties of $Ru_{1-x}Mo_x$ (x = 0.1-0.9) alloys

Yang Fu(付阳), Chunsheng Gong(龚春生), Zhijun Tu(涂志俊), Shangjie Tian(田尚杰), Shouguo Wang(王守国), and Hechang Lei(雷和畅)

Citation: Chin. Phys. B, 2024, 33 (**4**): 047404. DOI: 10.1088/1674-1056/ad2a73
Journal homepage: http://cpb.iphy.ac.cn; http://iopscience.iop.org/cpb

What follows is a list of articles you may be interested in

Coexistence of antiferromagnetism and unconventional superconductivity in a quasi-one-dimensional flat-band system: Creutz lattice

Feng Xu(徐峰) and Lei Zhang(张磊)
Chin. Phys. B, 2024, 33 (**3**): 037402. DOI: 10.1088/1674-1056/acf5d2

Effects of carrier density and interactions on pairing symmetry in a t_{2g} model

Yun-Xiao Li(李云霄), Wen-Han Xi(西文翰), Zhao-Yang Dong(董召阳), Zi-Jian Yao(姚子健), Shun-Li Yu(于顺利), and Jian-Xin Li(李建新)
Chin. Phys. B, 2024, 33 (**1**): 017404. DOI: 10.1088/1674-1056/ad1094

Ultralow-temperature heat transport study of noncentrosymmetric superconductor CaPtAs

Yimin Wan(万一民), Erjian Cheng(程二建), Yuxin Chen(陈宇鑫), Chengcheng Zhao(赵成成), Chengpeng Tu(涂成鹏), Dongzhe Dai(戴东喆), Xiaofan Yang(杨小帆), Lu Xin(辛路), Wu Xie(谢武), Huiqiu Yuan(袁辉球), and Shiyan Li(李世燕)
Chin. Phys. B, 2023, 32 (**12**): 127403. DOI: 10.1088/1674-1056/ad02e9

Effects of irradiation on superconducting properties of small-grained MgB_2 thin films

Li Liu(刘丽), Jung Min Lee, Yoonseok Han, Jaegu Song, Chorong Kim, Jaekwon Suk, Won Nam Kang, Jie Liu(刘杰), Soon-Gil Jung, and Tuson Park
Chin. Phys. B, 2023, 32 (**12**): 127402. DOI: 10.1088/1674-1056/acf5d3

Multi-band analysis on physical properties of superconducting FeSe films

Jian-Tao Che(车剑韬) and Chen-Xiao Ye(叶晨骁)
Chin. Phys. B, 2023, 32 (**9**): 097401. DOI: 10.1088/1674-1056/acd3e5

RAPID COMMUNICATION

Structure and superconducting properties of $Ru_{1-x}Mo_x$ ($x = 0.1$–0.9) alloys

Yang Fu(付阳)[1,2,†], Chunsheng Gong(龚春生)[1,2,†], Zhijun Tu(涂志俊)[1,2], Shangjie Tian(田尚杰)[3,1,2], Shouguo Wang(王守国)[3], and Hechang Lei(雷和畅)[1,2,‡]

[1] *Department of Physics and Beijing Key Laboratory of Opto-electronic Functional Materials & Micro-nano Devices, Renmin University of China, Beijing* 100872, *China*

[2] *Key Laboratory of Quantum State Construction and Manipulation (Ministry of Education), Renmin University of China, Beijing* 100872, *China*

[3] *Anhui Key Laboratory of Magnetic Functional Materials and Devices, School of Materials Science and Engineering, Anhui University, Hefei* 230601, *China*

(Received 21 December 2023; revised manuscript received 5 February 2024; accepted manuscript online 19 February 2024)

We report the detailed crystal structures and physical properties of $Ru_{1-x}Mo_x$ alloys in the solid solution range of $x = 0.1$–0.9. Structure characterizations indicate that the crystal structure changes from the hcp-Mg-type, to β-CrFe-type, and then bcc-W-type. The measurements of physical properties show that the $Ru_{1-x}Mo_x$ samples with $x \geq 0.2$ are superconductors and the superconducting transition temperature T_c as a function of Mo content exhibits a dome-like behavior.

Keywords: superconductivity, alloy, crystal structures, $Ru_{1-x}Mo_x$

PACS: 74.25.–q, 74.70.Ad, 74.62.–c, 74.25.F– **DOI:** 10.1088/1674-1056/ad2a73

1. Introduction

The spin–orbit coupling (SOC) effect originates from the interaction between electron's spin and orbit degrees of freedom, and it has been widely studied in condensed matter physics, especially in the field of topological physics. The SOC effect can lift the degeneracy of electronic band structure and plays a critical role in exploring different topological states, such as topological insulators and topological semimetals.[1–3] In addition, the SOC effect also has an influence on the superconducting materials and can induce unconventional superconductivity. For example, in quasi-two-dimensional or noncentrosymmetric superconductors it can promote and stabilize superconductivity,[4] allow the mixture of spin-singlet and spin-triplet pairing,[5] or even increase superconducting transition temperature T_c.[6] Thus, it is promising to discover novel superconductors with unconventional properties in the materials with strong SOC effect.

It is well known that the atomic SOC is proportional to Z^4, where Z is the nuclear charge number, and thus increases with the increase of Z quickly. Compared to 3d transition metal compounds, the 4d and 5d transition metal compounds exhibit significant advantages, especially 5d compounds. For instance, compared with 4d elements Pd, the larger Z value of 5d element Pt makes Li_2Pt_3B exhibit a mixed pairing state of spin singlet and spin triplet, while Li_2Pd_3B with the same structure does not show similar characteristics.[7] Furthermore, many noncentrosymmetric superconductors with strong SOC effect, such as BiPd, YPtBi and $PbTaSe_2$, have been extensively investigated as candidates of topological superconductors.[8–10]

On the other hand, because of their relatively high T_c and specially structural properties, some compound superconductors consisting of 4d element Mo have attracted much attention, such as MoC (the highest $T_c = 14.3$ K) and $Re_{1-x}Mo_x$ ($0 < x < 1$) ($T_c = 3$–12 K) with relatively high T_c,[11] noncentrosymmetric superconductors Mo_3Al_2C ($T_c = 9.4$ K) and Mo_3Rh_2N ($T_c = 4.3$ K),[12,13] possible unconventional superconductor Mo_8Ga_{41} ($T_c = 9.8$ K),[14] as well as Mo_3Sb_7 ($T_c = 2.3$ K) with possible coexistence of superconductivity and spin fluctuations.[15] By studying the specific heat of Mo and some Mo-based compounds, Morin and Maita found that d electrons play a very important role in Mo-based superconductors.[16] Theoretical studies also suggest that phonon-induced d–d electron coupling has a certain influence on the T_c of the transition metal.[17]

Motivated by these studies, we carried out a detailed investigation on the series of $Ru_{1-x}Mo_x$ ($x = 0.1$–0.9) alloys. Although the superconductivity of some $Ru_{1-x}Mo_x$ alloys has been reported in the literature,[18,19] a systematic study of physical properties for the whole series of $Ru_{1-x}Mo_x$ ($x = 0.1$–0.9) is still lacking. The present work provides a detailed superconducting phase diagram in the solid solution range of $Ru_{1-x}Mo_x$ ($x = 0.1$–0.9) and the detailed physical properties of $Ru_{0.5}Mo_{0.5}$ with T_c about 9.71 K.

[†]These authors contributed equally to this work.

[‡]Corresponding author. E-mail: hlei@ruc.edu.cn

© 2024 Chinese Physical Society and IOP Publishing Ltd

2. Experimental details

$Ru_{1-x}Mo_x$ ($x = 0.1$–0.9) polycrystals were synthesized by the arc-melting method in the high-purity argon atmosphere. Powders of pure Mo (99.9%) and Ru (99.9%) were mixed with different stoichiometric ratios using a mortar and then pressed into pellets. The arc-melted buttons were flipped over and remelted several times to improve the homogeneity of samples. The weight losses during arc melting were negligible for all samples. The as-cast ingots were used in this study without undergoing a further annealing process. The chemical compositions of samples were characterized by energy-dispersive x-ray spectroscopy (EDX). Crystal structure and phase purity were examined by powder x-ray diffraction pattern (PXRD) with Cu K_α radiation ($\lambda = 0.15418$ nm) using a Bruker D8 x-ray diffractometer. The lattice parameters were extracted by fitting the PXRD pattern using the TOPAS4 software.[20] Electrical transport and specific heat measurements were performed using a Quantum Design PPMS-14T. Magnetization measurements were carried out using a Quantum Design MPMS3.

3. Results and discussion

Figure 1(a) shows the actual Mo concentration x_{EDX} determined by EDX measurement on the polished samples as a function of the nominal value x_{nom}. It can be seen that there is a linear relationship between x_{nom} and x_{EDX}, suggesting that the actual Mo concentration in $Ru_{1-x}Mo_x$ ($x = 0.1$–0.9) is close to the nominal one and the Ru–Mo binary system can form a continuous solid solution in the whole range. Thus, x_{EDX} (denoted as x) will be used for the following discussion. Figures 1(b)–1(d) show three typical PXRD patterns and crystal structures (insets) of $Ru_{1-x}Mo_x$ ($x = 0.5$, 0.6 and 0.9). No extra diffraction peaks are detected, indicating high quality of the samples. On the Ru-rich side, $Ru_{1-x}Mo_x$ has a hexagonal close packing Mg (hcp-Mg) type structure (space group $P6_3/mmc$). The results of XRD refinement confirm that all the samples with $0 \le x \le 0.5$ exhibit hcp-Mg-type structure. When $0.5 < x \le 0.7$, the samples exhibit the tetragonal β-CrFe (space group $P4_2/mnm$) and body-centered-cubic W (bcc-W) type (space group $Im\text{-}3m$) structures, mixed with the hcp-Mg-type structure. It suggests that there is a phase separation within this composition range. Further increasing the content of Mo, the structure of $Ru_{1-x}Mo_x$ changes to the bcc-W-type completely. Figure 1(e) shows the fitted lattice parameters obtained from the Rietveld refinement. On the Ru-rich side, both a- and c-axial lattice parameters increase slightly with increasing x. For the β-CrFe-type $Ru_{1-x}Mo_x$, a- and c-axial values show nonmonotonic changes. On the Mo-rich side, the a-axial value of bcc-W-type structure increases gradually again with increasing x. These results are consistent with the larger atomic radius of Mo than that of Ru in principle.

Figure 2(a) shows the temperature dependence of zero-field electrical resistivity $\rho(T)$ for $Ru_{1-x}Mo_x$ ($x = 0.1$–0.9) from 2 K to 300 K. All samples exhibit a metallic behavior and the room-temperature resistivity $\rho_{300\,K}$ as a function of x

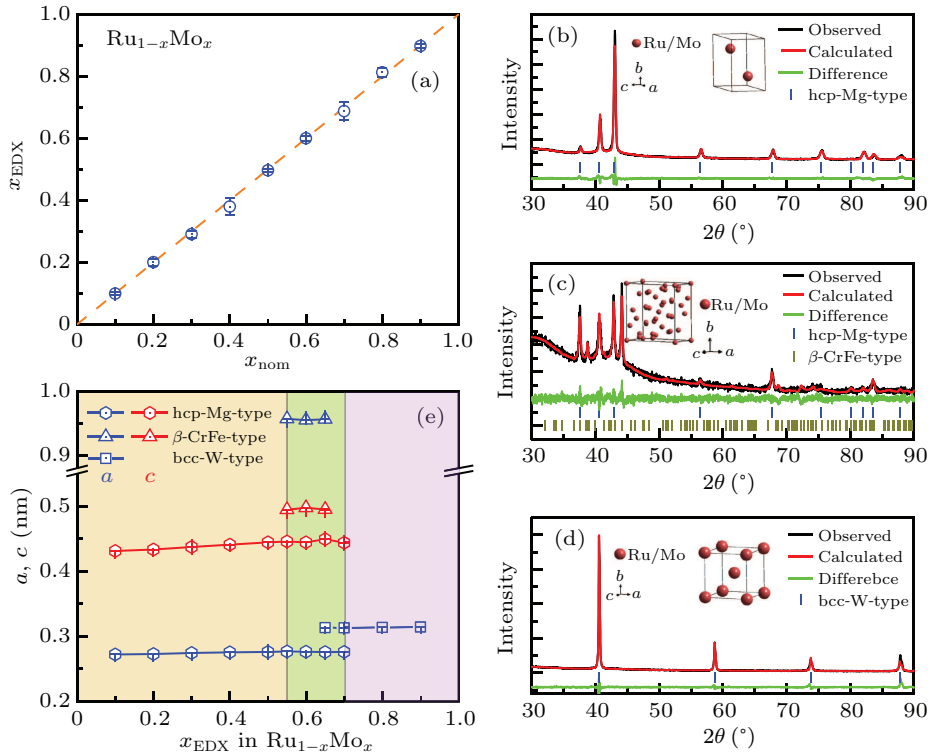


Fig. 1. (a) Relationship between the nominal concentration of Mo x_{nom} and the actual one x_{EDX} determined by EDX in $Ru_{1-x}Mo_x$ ($x = 0.1$–0.9) polycrystals. (b)–(d) Room-temperature PXRD patterns and refinements for $Ru_{0.5}Mo_{0.5}$, $Ru_{0.4}Mo_{0.6}$ and $Ru_{0.1}Mo_{0.9}$, respectively. (e) The lattice parameters a and c as a function of Mo content in $Ru_{1-x}Mo_x$.

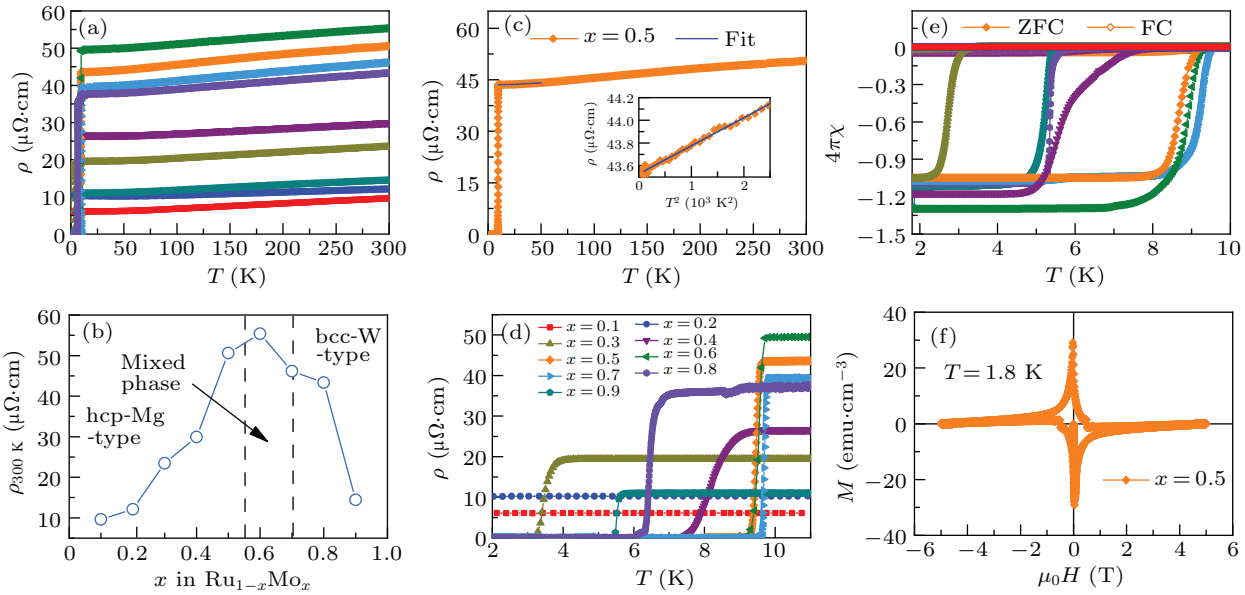


Fig. 2. (a) Temperature dependence of electrical resistivity $\rho(T)$ for $Ru_{1-x}Mo_x$ ($x = 0.1$–0.9) polycrystals at zero field. (b) $\rho_{300\ K}$ as a function of x. (c) The $\rho(T)$ of $Ru_{0.5}Mo_{0.5}$ polycrystal at zero field. Inset: enlarged view of the fit in the range of 2–50 K. The blue solid lines represent the fits using the formula $\rho(T) = \rho_0 + AT^2$. (d) Enlarged view of $\rho(T)$ below $T = 11$ K. (e) Temperature dependence of magnetic susceptibility $4\pi\chi(T)$ measured at 1 mT with ZFC and FC modes. (f) The magnetization hysteresis loop measured at $T = 1.8$ K for the sample with $x = 0.5$. The color code in all figures except (b) is the same.

is summarized in Fig. 2(b). For the sample with $x \leq 0.5$, the $\rho_{300\ K}$ increases gradually with increasing Mo concentration, but with further increasing the content of Mo ($x \geq 0.6$), the $\rho_{300\ K}$ starts to decrease. It implies that the electron–phonon scattering may be strongest when x is close to 0.6. When the temperature is below 50 K, the $\rho(T)$ curves for all samples can be fitted well by using the formula $\rho(T) = \rho_0 + AT^2$, where ρ_0 is the residual resistivity, and A is the coefficient of electron–electron scattering. The example of $Ru_{0.5}Mo_{0.5}$ is shown in Fig. 2(c). It implies that the dominant scattering mechanisms at low-temperature region are electron–electron and electron–impurity ones, and the $Ru_{1-x}Mo_x$ system exhibits a Fermi liquid behavior in this temperature range.

Figure 2(d) shows the enlarged view of $\rho(T)$ data at $T \leq 11$ K and all samples with $x \geq 0.3$ exhibit obvious superconducting transitions. The onset superconducting transition temperature T_c^{onset} determined as the temperature at which the resistivity starts to decrease exhibits a non-monotonic variation with x and reaches a maximum value of 9.71 K for the single-phase sample with $x = 0.5$. The bulk superconductivity in $Ru_{1-x}Mo_x$ ($x = 0.1$–0.9) is confirmed by magnetization measurements. As shown in Fig. 2(e), a clear diamagnetic signal in magnetic susceptibility $4\pi\chi(T)$ curves can be observed for the samples with $x \geq 0.3$. The T_c^{onset}s are also consistent with those obtained from the resistivity measurements. For the sample with $x = 0.2$, there is a weak drop near 2.10 K, suggesting that there is a superconducting transition at lower temperature beyond the present measuring range. In addition, for the samples with $x = 0.6$ and 0.7, the $4\pi\chi(T)$ curves show a behavior of two-step transition, which can be ascribed to the coexistence of two superconducting phases as shown in Fig. 1(e). Without demagnetization corrections, the superconducting volume fractions estimated from the zero-field-cooling (ZFC) $4\pi\chi(T)$ curves at $T = 2$ K exceed 100%, indicating the bulk superconductivity for the samples with $x \geq 0.3$. For all superconducting samples, they show a bifurcation behavior of ZFC and field-cooling (FC) $4\pi\chi(T)$ curves due to the flux pinning effect, which is a typical feature of type-II superconductors. The type-II superconductivity is further confirmed by the magnetic hysteresis loops measured at 1.8 K and Fig. 2(g) shows an example for the sample with $x = 0.5$.

To gain further insight into the superconducting properties of $Ru_{1-x}Mo_x$, we carried out comprehensive characterizations for the $x = 0.5$ sample which is pure and has the optimal T_c among the single-phase samples. Figure 3(a) shows the temperature dependence of $\rho(T)$ at various fields up to 11 T. The T_c is gradually suppressed to the lower temperature but the width of superconducting transition only increases slightly, implying the weak flux pinning effect in $Ru_{0.5}Mo_{0.5}$. Figure 3(b) shows the upper critical field $\mu_0 H_{c2}(T)$ corresponding to the temperatures where the resistivity drops to 50% of the normal state resistivity just above the onset of superconductivity transition. The $\mu_0 H_{c2}(T)$ curve can be well fitted by using the Werthamer–Helfand–Hohenberg (WHH) equation without considering the effects of Pauli spin paramagnetism and spin–orbit interaction.[21] The fitted zero-temperature upper critical field $\mu_0 H_{c2}(0)$ is 9.856(7) T and this value is much smaller than the Pauli limited field $\mu_0 H_{c2}^P(0) = 1.84 T_c = 17.866$ T, indicating that the orbital pairing-broken mechanism is dominant in $Ru_{0.5}Mo_{0.5}$.

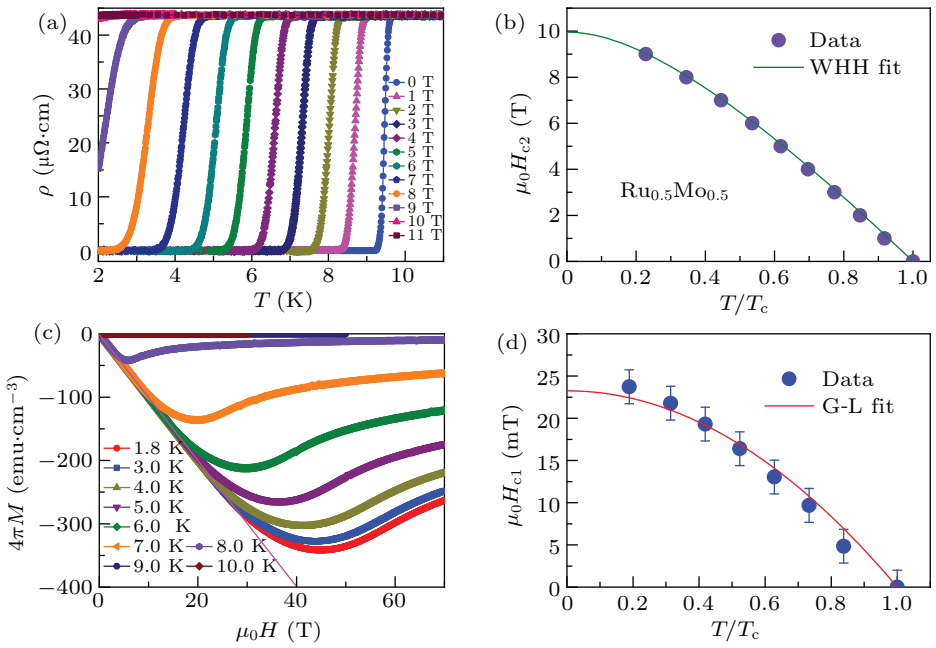


Fig. 3. (a) The $\rho(T)$ as a function of temperature at various fields for $Ru_{0.5}Mo_{0.5}$. (b) Temperature dependence of $\mu_0 H_{c2}(T)$. The green solid line represents the fit using the WHH formula. (c) Low-field dependence of magnetization $4\pi M(\mu_0 H)$ at various temperatures below T_c. The pink solid line represents the Meissner line. (d) $\mu_0 H_{c1}(T)$ as a function of T/T_c. The red line represents the fit using the G-L equation.

Figure 3(c) exhibits the low-field dependence of magnetization $4\pi M(\mu_0 H)$ at various temperatures below T_c for $Ru_{0.5}Mo_{0.5}$. When the field is smaller than the lower critical field $\mu_0 H_{c1}$, the sample is in the Meissner state and the $4\pi M(\mu_0 H)$ curve is expected to be linear with slope $4\pi M/H = -1$ ("Meissner line"). For $\mu_0 H > \mu_0 H_{c1}$, magnetic flux starts to penetrate into the sample and the magnetization curve begins to deviate from the linearly field-dependent behavior. In order to estimate the $\mu_0 H_{c1}(T)$ accurately, the effective field $\mu_0 H_{eff}$ is calculated using the formula $\mu_0 H_{eff} = \mu_0 H - N_d M$, where N_d is the demagnetization factor. The estimated N_d is 0.074 by using the geometry size of the rectangular sample. The $\mu_0 H_{c1}(T)$ determined by the above method as a function of temperature is presented in Fig. 3(d). The temperature dependence of $\mu_0 H_{c1}(T)$ can be well fitted by the Ginzburg–Landau (G-L) equation $\mu_0 H_{c1}(T) = \mu_0 H_{c1}(0)[1 - (T/T_c)^2]$, where $\mu_0 H_{c1}(0)$ is the value of $\mu_0 H_{c1}$ at zero temperature. The fit gives $\mu_0 H_{c1}(0) = 23.25(6)$ mT. By using the following two formulas:

$$\xi_{GL} = \left(\frac{\phi_0}{2\pi\mu_0 H_{c2}(0)}\right)^{\frac{1}{2}}, \quad \mu_0 H_{c1} = \frac{\phi_0}{4\pi\lambda_{GL}^2}\ln\frac{\lambda_{GL}}{\xi_{GL}},$$

where ϕ_0 is the magnetic flux quantum ($h/(2e) = 2.07 \times 10^{-15}$ Wb), the derived G-L coherence length ξ_{GL} and penetration depth λ_{GL} are 5.782(2) nm and 152.22(3) nm, respectively. Correspondingly, the calculated G-L parameter $\kappa_{GL} = \lambda_{GL}/\xi_{GL} = 26.33(4)$, confirming the type-II superconductivity in $Ru_{0.5}Mo_{0.5}$. The zero-temperature thermodynamic critical field $\mu_0 H_c(0)$ is estimated to be 295(5) mT using the formula $\mu_0 H_c(0) = [\mu_0 H_{c1}(0)\mu_0 H_{c2}(0)/\ln\kappa_{GL}]^{1/2}$.

The bulk superconductivity of $Ru_{0.5}Mo_{0.5}$ is also confirmed by the specific heat measurement shown in Fig. 4(a). The thermodynamic T_c^{onset} defined as the temperature at which C_p begins to jump is 9.71 K, close to the values obtained from the $\rho(T)$ and $\chi(T)$ curves. Furthermore, with increasing field, the specific-heat jump gradually shifts to lower temperatures and when $\mu_0 H > 10$ T, no superconducting transition can be observed at $T > 2$ K, consistent with the $\rho(T)$ measurement. Figure 4(b) shows the enlarged view of C_p/T curve at $\mu_0 H = 12$ T. In order to obtain the electronic specific heat coefficient γ and Debye temperatures Θ_D, the curves are fitted using the equation $C_p(T)/T = \gamma + \beta T^2$. The extracted γ is 4.53(4) mJ·mol^{-1}·K^{-2} and β is 0.0355(8) mJ·mol^{-1}·K^{-4}. Furthermore, the calculated Θ_D is 380(4) K by using the formula $\Theta_D = (12\pi^4 NR/5\beta)^{1/3}$, where N (= 1) is the number of atoms per formula unit and R (= 8.314 J·mol^{-1}·K^{-1}) is the ideal gas constant. According to the McMillan formula for electron–phonon-mediated superconductivity,[22] the electron–phonon coupling constant λ_{e-ph} can be determined by the formula

$$\lambda_{e-ph} = \frac{1.04 + \mu^* \ln\left(\frac{\Theta_D}{1.45T_c}\right)}{(1 - 0.62\mu^*)\ln\left(\frac{\Theta_D}{1.45T_c}\right) - 1.04}, \quad (1)$$

where $\mu^* = 0.13$ is the common value for Coulomb pseudopotential. Using the above values of T_c^{onset} and Θ_D, the estimated λ_{e-ph} is 0.738(3), indicating that $Ru_{0.5}Mo_{0.5}$ is a weakly or moderately coupled superconductor. Figure 4(c) shows the temperature dependence of electronic specific heat C_e obtained by subtracting the phonon contribution from the total specific

heat. The estimated specific heat jump $\Delta C_e(T)/(\gamma T_c^{onset})$ of $Ru_{0.5}Mo_{0.5}$ is 1.06, slightly smaller than the BCS value of 1.43. Furthermore, we find that the normalized electronic specific heat $C_e/(\gamma T)$ as a function of the reduced temperature T/T_c^{onset} can be well fitted with the equation $C_e/(\gamma T) = ae^{-bT_c^{onset}/T}$, where a is a temperature-independent constant. The result gives $a = 7.75(5)$ and $b = 0.948(4)$. By using $\Delta(0) \approx 1.22b$, where $\Delta(0)$ is the zero-temperature superconducting gap,[23] we obtain $2\Delta(0)/(k_B T_c) = 2.313(9)$, which is smaller than the BCS value of 3.52. It suggests a weakly coupled superconductivity in $Ru_{0.5}Mo_{0.5}$. All physical parameters of $Ru_{0.5}Mo_{0.5}$ are summarized in Table 1. Figure 4(d) shows the zero-field electronic specific heat plotted as $C_e/(\gamma T_c)$ for all $Ru_{1-x}Mo_x$ samples ($x = 0.1$–0.9) at the low temperature region. A clear specific heat jump can be observed in all samples with $x \geq 0.3$, confirming the bulk nature of superconductivity in $Ru_{1-x}Mo_x$ ($x = 0.3$–0.9). In addition, there are two jumps for the samples with $x = 0.6$ and 0.7, indicating the existence of phase separation in this composition range. Using the similar analysis procedure to that for $Ru_{0.5}Mo_{0.5}$, the relevant superconducting thermodynamic parameters are summarized in Table 2. It can be seen that in the whole range of x, $Ru_{1-x}Mo_x$ should be weakly or moderately coupled BCS superconductors.

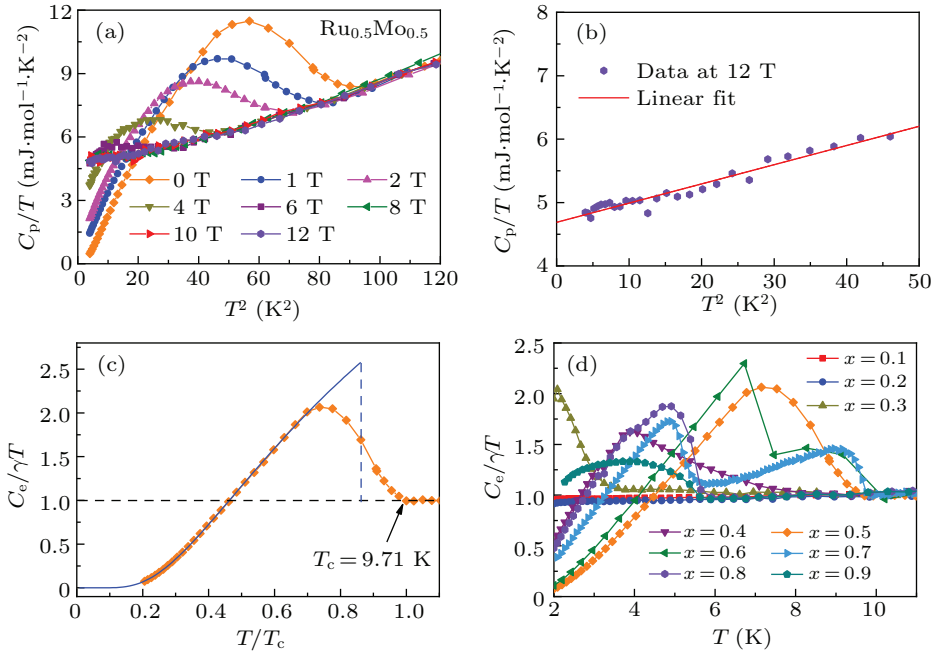


Fig. 4. (a) The C_p/T vs. T^2 at various fields for $Ru_{0.5}Mo_{0.5}$. (b) C_p/T vs. T^2 at $\mu_0 H = 12$ T. The red solid line represents the linear fit using the equation $C_p(T)/T = \gamma + \beta T^2$. (c) Temperature dependence of electronic specific heat plotted as $C_e/(\gamma T)$ vs. T/T_c^{onset} at zero field. The solid line represents the fitting result using the formula $C_e/(\gamma T) = ae^{-bT_c^{onset}/T}$. (d) Temperature dependence of $C_e/(\gamma T)$ at zero field for $Ru_{1-x}Mo_x$ ($x = 0.1$–0.9).

Table 1. Physical parameters of $Ru_{0.5}Mo_{0.5}$ at superconducting and normal states.

Parameter	Unit	Value
T_c^{onset}	K	9.71
$\mu_0 H_{c1}(0)$	mT	23.25(6)
$\mu_0 H_{c2}(0)$	T	9.856(7)
$\mu_0 H_c(0)$	T	0.295(5)
ξ_{GL}	nm	5.782(2)
λ_{GL}	nm	152.22(3)
κ_{GL}	–	26.33(4)
γ	mJ·mol^{-1}·K^{-2}	4.53(4)
Θ_D	K	380(4)
$\Delta C_e/(\gamma T_c^{onset})$	–	1.06
λ_{e-ph}	–	0.738(3)
$2\Delta(0)/(k_B T_c^{onset})$	–	2.313(9)

Based on the above experimental data, the superconducting phase diagram of the $Ru_{1-x}Mo_x$ as a function of the Mo concentration is shown in Fig. 5(a). The T_c values determined from resistivity, magnetization and specific heat measurements are consistent with each other. It can be seen that with the increase of Mo concentration, the T_c changes nonmonotonically. When $x \leq 0.5$, the T_c gradually increases with the increase of Mo content. With further increasing x larger than 0.7, the T_c decreases rapidly. For transition metals, an empirical rule proposed by Matthias exists between T_c and the average number of valence electrons per atom n,[18] i.e., the T_c is expected to exhibit two maxima at n close to 5 and 7. Such behavior might be related to the unique shape of the density of states $N(E)$, which exhibits sharp peaks corresponding to these electron numbers.[24] For the series of $Ru_{1-x}Mo_x$, the n increases from 6 for pure Ru to 8 for pure Mo, and for $x = 0.5$, this value is 7. Thus, the dome-like behavior of T_c can be explained well by this rule. We have also calculated the Kadowaki–Woods ratio $\sigma = A/\gamma^2$ using the fitted A and γ for resistivity and specific heat measurements[25] and the values are listed in Table 2. A

comparison of our results with those of previous systems[26] is also illustrated in Fig. 5(b). It can be seen that the values of $Ru_{1-x}Mo_x$ series are higher than those of transition metals ($\sigma_{TM} \sim 0.4$ μΩ·cm·mol^2·K^2·J^{-2}). Notably, the values for the samples with $x = 0.5$, 0.6, and 0.7 are close to those of heavy fermion materials ($\sigma_{HF} \sim 10$ μΩ·cm·mol^2·K^2·J^{-2}). It suggests that there may be a strong electron–electron correlation effect in $Ru_{1-x}Mo_x$ system when x is close to 0.5. However further experimental and theoretical studies are needed to confirm this effect in the future.

Table 2. Physical parameters of $Ru_{1-x}Mo_x$ ($x = 0.1$–0.9).

x	T_c^{onset} (K)	γ (mJ·mol^{-1}·K^{-2})	β (mJ·mol^{-1}·K^{-4})	Θ_D (K)	$\Delta C_e/(\gamma T_c^{onset})$	λ_{e-ph}	A (μΩ·cm·K^{-2})	$\sigma = A/\gamma^2$ (μΩ·cm·mol^2·K^2·J^{-2})
0.1	–	3.17(2)	0.0070(1)	652(3)	–	–	$0.36(2)\times10^{-4}$	3.6(2)
0.2	–	3.24(1)	0.01521(3)	503(7)	–	–	$0.13(1)\times10^{-4}$	1.2(1)
0.3	3.78	3.05(2)	0.0144(9)	513(11)	1.06	0.520(2)	$0.37(4)\times10^{-4}$	4.0(4)
0.4	9.37	3.86(5)	0.0110(8)	561(14)	0.62	0.640(5)	$0.15(3)\times10^{-4}$	1.0(2)
0.5	9.71	4.53(4)	0.0355(8)	380(4)	1.06	0.738(3)	$2.47(4)\times10^{-4}$	12.0(2)
0.6	10.21	3.87(6)	0.037(3)	375(10)	–	0.756(8)	$2.2(2)\times10^{-4}$	15(1)
0.7	9.85	2.70(4)	0.0508(3)	337(1)	–	0.778(1)	$1.50(6)\times10^{-4}$	21(1)
0.8	5.91	4.04(3)	0.033(1)	389(4)	0.88	0.622(2)	$1.00(7)\times10^{-4}$	6.1(4)
0.9	5.62	3.35(3)	0.020(1)	460(8)	0.33	0.586(3)	$0.53(2)\times10^{-4}$	4.7(2)

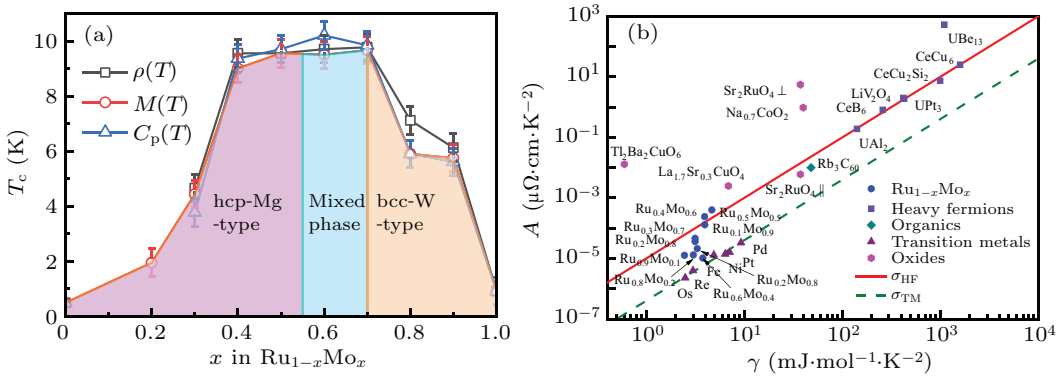


Fig. 5. (a) Superconducting phase diagram of the $Ru_{1-x}Mo_x$. (b) Kadowaki–Woods plot for various superconductors. The red solid line represents $\sigma_{HF} = 10$ μΩ·cm·mol^2·K^2·J^{-2} and the green dashed line represents $\sigma_{TM} = 0.4$ μΩ·cm·mol^2·K^2·J^{-2}.

4. Conclusion

In summary, we successfully synthesized a series of $Ru_{1-x}Mo_x$ ($x = 0.1$–0.9) alloys using the arc-melting method. There are three different structures existing in $Ru_{1-x}Mo_x$ alloys, including hcp-Mg-type, β-CrFe-type and W-type structures. Systematic physical property measurements show that the $Ru_{1-x}Mo_x$ samples with $x \geq 0.2$ exhibit superconductivity with T_c above 2 K and they are type-II weakly or moderately coupled BCS superconductors. Interestingly, there is a dome-like superconducting phase diagram. This behavior is consistent with the Matthias rule that the T_c is expected to exhibit two maxima at n close to 5 and 7.

Acknowledgements

Project supported by Beijing Natural Science Foundation (Grant No. Z200005), the National Key R&D Program of China (Grant Nos. 2018YFE0202600 and 2022YFA1403800), the National Natural Science Foundation of China (Grant No. 12274459), Beijing National Laboratory for Condensed Matter Physics, and Collaborative Research Project of Laboratory for Materials and Structures, Institute of Innovative Research, Tokyo Institute of Technology.

References

[1] Qi X L and Zhang S C 2011 *Rev. Mod. Phys.* **83** 1057
[2] Hasan M Z and Kane C L 2010 *Rev. Mod. Phys.* **82** 3045
[3] Armitage N P, Mele E J and Vishwanath A 2018 *Rev. Mod. Phys.* **90** 015001
[4] Caviglia A D, Gabay M, Gariglio S, Reyren N, Cancellieri C and Triscone J M 2010 *Phys. Rev. Lett.* **104** 126803
[5] Gor'kov L P and Rashba E I 2001 *Phys. Rev. Lett.* **87** 037004
[6] Gardner H J, Kumar A, Yu L, Xiong P, Warusawithana M P, Wang L, Vafek O and Schlom D G 2011 *Nat. Phys.* **7** 895
[7] Nishiyama M, Inada Y and Zheng G Q 2005 *Phys. Rev. B* **71** 220505
[8] Bian G, Chang T R, Sankar R, Xu S Y, Zheng H, Neupert T, Chiu C K, Huang S M, Chang G, Belopolski I, *et al.* 2016 *Nat. Commun.* **7** 10556
[9] Sun Z, Enayat M, Maldonado A, Lithgow C, Yelland E, Peets D C, Yaresko A, Schnyder A P and Wahl P 2015 *Nat Commun.* **6** 6633
[10] Kim H, Wang K, Nakajima Y, Hu R, Ziemak S, Syers P, Wang L, Hodovanets H, Denlinger J D, Brydon P M R, Agterberg D F, Tanatar M A, Prozorov R and Paglione J 2018 *Sci. Adv.* **4** eaao4513
[11] Shang T, Gawryluk D J, Verezhak J A T, Pomjakushina E, Shi M, Medarde M, Mesot J and Shiroka T 2019 *Phys. Rev. Mater.* **3** 024801

[12] Bauer E, Rogl G, Chen X Q, Khan R T, Michor H, Hilscher G, Royanian E, Kumagai K, Li D Z, Li Y Y, Podloucky R and Rogl P 2010 *Phys. Rev. B* **82** 064511
[13] Wei W, Zhao G J, Kim D R, Jin C, Zhang J L, Ling L, Zhang L, Du H, Chen T Y, Zang J, Tian M, Chien C L and Zhang Y 2016 *Phys. Rev. B* **94** 104503
[14] Bezinge A and Yvon K 1984 *J. Less-Common. Met.* **99** L27
[15] Bukowski Z, Badurski D, Stepien-Damm J and Troc R 2002 *Solid State Commun.* **123** 283
[16] Morin F J and Maita J P 1963 *Phys. Rev.* **129** 1115
[17] Poon S J 1976 *Solid State Commun.* **18** 1489
[18] Matthias B T 1955 *Phys. Rev.* **97** 74
[19] Flewitt P E J and Tate A J 1972 *Less Common Metals* **27** 339
[20] TOPAS Version 4; Bruker AXS, Karlsruhe, Germany 2007
[21] Werthamer N R, Helfand E and Hohenberg P C 1966 *Phys. Rev.* **147** 295
[22] McMillan W L 1968 *Phys. Rev.* **167** 331
[23] Johnston D C 2013 *Supercond. Sci. Technol.* **26** 115011
[24] Iyo A, Yanagi Y, Kinjo T, Nishio T, Hase I, Yanagisawa T, Ishida S, Kito H, Takeshita N, Oka K, Yoshida Y and Eisaki H 2015 *Sci. Rep.* **5** 10089
[25] Kadowaki K and Woods S B 1986 *Solid State Commun.* **58** 507
[26] Jacko A C, Fjærestad J O and Powell B J 2009 *Nat. Phys.* **5** 422